Journal of Materials Chemistry A

PAPER

View Article Online
View Journal | View Issue

Cite this: J. Mater. Chem. A, 2019, 7, 11086

A C_{60}/TiO_x bilayer for conformal growth of perovskite films for UV stable perovskite solar cells†

Cheng Liu,‡[a] Molang Cai,‡[a] Yi Yang,[a] Zulqarnain Arain,[ab] Yong Ding,*[a] Xiaoqiang Shi,[a] Pengju Shi,[a] Shuang Ma,[a] Tasawar Hayat,[c] Ahmed Alsaedi,[c] Jihuai Wu,[d] Songyuan Dai*[ac] and Guozhong Cao*[e]

Perovskite solar cells (PSCs) have been widely studied and such research resulted in high power conversion efficiency (PCE). However, stability remains a great challenge when TiO_2 or other wide bandgap n-type oxide semiconductors are used as the electron transport layer (ETL). The use of carbon such as fullerene (C_{60}) as an ETL has shown promise with much improved UV stability. But there are two major obstacles to overcome: the first is the difficulty to fabricate C_{60} films with full coverage mainly due to the low solubility of fullerene in dichlorobenzene and the second is the hydrophobicity of C_{60} that hinders the deposition of pin hole free perovskite films with high crystallinity, intimate contact, and a desired columnar microstructure. In this work, a C_{60}/ultrathin-TiO_x (u-TiO_x) bilayer is designed and fabricated as a compact ETL, which restrains the charge recombination at the ETL/perovskite interface and significantly enhances the PSC UV stability. Not only does the introduction of TiO_x on top of the C_{60} film fill the holes or gaps in the C_{60} film, but also it enhances the surface energy benefiting the growth of perovskite with an intimate contact between the ETL and perovskite, which results in an enhanced perovskite crystallization and a reduced charge recombination at the interface. Both the open-circuit voltage and fill factor were largely improved to obtain a PCE of 19.38% with a rigid device. The highest efficiency 14.74% of a larger-area flexible PSC (1.0 cm^2) based on the bilayer was obtained due to the superior homogeneity of the films. More importantly, by eliminating the negative charge accumulation at the perovskite/ETL interface and suppressing the irreversible moisture-driven decomposition of perovskite materials, the C_{60}/u-TiO_x bilayer-based PSC shows outstanding stability, retaining 83% and 90% of its initial performance after 312 h UV irradiation and 1000 h exposure to ambient air, respectively.

Received 25th February 2019
Accepted 26th March 2019

DOI: 10.1039/c9ta02094b

rsc.li/materials-a

1. Introduction

Perovskite solar cells (PSCs) have attracted enormous research interest in recent years due to their rapidly rising efficiency along with the advantage of very low material costs. The highest efficiency of beyond 23% was reported in work based on n–i–p structured PSCs.[1–3] The high efficiencies and low-temperature solution-processed perovskite film make n–i–p PSCs a very promising candidate for efficient and flexible photovoltaic devices. However, a high-temperature processed (>450 °C) electron transport layer (ETL) is usually required for achieving high performance of PSCs, which hinders the development of flexible perovskite devices.

To overcome these limitations, various low-temperature (<150 °C) solution-processed materials have been exploited as ETLs, such as metal oxide materials (ZnO, SnO_2, WO_X, Zn_2SnO_4, and La-$BaSnO_3$) and organic materials (solid-state ionic-liquids and PCBM).[4–14] Among these materials, fullerene (C_{60}), owing to its outstanding properties such as unusual high electron-mobility and extreme stability, has entered the low-temperature processed ETL field as an emerging contender, benefiting from the internal–external double spherical π electron cloud, highest central symmetry in three-dimensional Euclidean space and lack of molecular defects.[15,16] However, the poor coverage of C_{60} using solution based fabrication processes results in significant charge recombination and excessive electron accumulation at the interface of the ETL and perovskite layer.[17] The efficiency of n–i–p structured PSCs fabricated by such non-uniform films is inadequate.[18] Using an

[a]State Key Laboratory of Alternate Electrical Power System with Renewable Energy Sources, North China Electric Power University, Beijing 102206, P. R. China. E-mail: dingy@ncepu.edu.cn; sydai@ncepu.edu.cn

[b]Energy System Engineering Department, Sukkur IBA University, Sukkur, Pakistan

[c]NAAM Research Group, Department of Mathematics, Faculty of Science, King Abdulaziz University, Jeddah, 21589, Saudi Arabia

[d]Fujian Provincial Key Laboratory of Photoelectric Functional Materials, Institute of Materials Physical Chemistry, Huaqiao University, Xiamen 361021, China

[e]Institute of Materials Science & Engineering, University of Washington, Seattle, 98195, USA. E-mail: gzcao@uw.edu

† Electronic supplementary information (ESI) available. See DOI: 10.1039/c9ta02094b

‡ These authors contributed equally to this work.

evaporation technique can largely improve the coverage of C_{60} films.[19,20] Nevertheless, the unsatisfactory morphology of perovskite films with pinholes, as formed on the hydrophobic C_{60} surface, leads to both a relatively low fill factor and low open-circuit voltage of devices. It must also be considered that some anti-solvents (*e.g.*, chlorobenzene and toluene) can dissolve the underlying C_{60} ETL during the spin-coating process of the perovskite. Thus, the device based on the C_{60} substrate is not reproducible when reported for application in large-area devices (>1 cm^2).[21] It is critical to develop a modified interfacial layer to reduce the surface energy of the C_{60} film and resist corrosion by the anti-solvent. Low-temperature processed TiO_x has been widely used as an ETL which shows good performance and reproducibility in large area devices. It is mainly due to the good band alignment and hydrophilic nature of TiO_x, which can facilitate the growth of pinhole free perovskite films. Besides, using *in situ* synthesis techniques, such as $TiCl_4$ chemical bath deposition (CVD) and atomic layer deposition (ALD), can result in improved contact between the ETL and conductive glass for large areas.[22,23] However, unlike C_{60}, the low-temperature processed TiO_x still suffers from low electron mobility and high density of deep charge traps, inducing strong hysteresis behavior and rapid performance degradation in PSCs.

In this study, $TiCl_4$ chemical bath deposition performed under near room temperature conditions is preferred to fabricate the interfacial bilayer with a heat-sensitive C_{60} film for achieving a large-area high performance device. A low-temperature-processed (<70 °C) C_{60}/ultrathin-TiO_x (u-TiO_x) bilayer was successfully designed as an ETL to fabricate large-area (1 cm^2) flexible PSCs. The C_{60}/u-TiO_x bilayer completely covers the conductive substrate and dramatically improves the surface energy of the ETL. The intimate contact between the ETL and perovskite layer enhances the charge transport and avoids the electron accumulation at the interface. Meanwhile, the perovskite film deposited on the bilayer exhibits much fewer defects and suppressed charge recombination, because the reduced nucleation Gibbs free energy (ΔG) of perovskite seeds is beneficial to fabricate high-quality perovskite layers. As a result, the rigid and flexible PSCs show PCEs of 19.38% and 14.7% without hysteresis, respectively, for an aperture area of 1 cm^2. Moreover, by removing the negative charge accumulation at the perovskite/ETL interface and suppressing the irreversible moisture-driven decomposition of perovskite materials, the PSC based on the C_{60}/u-TiO_x bilayer shows outstanding stability, retaining 83% of its initial performance after 312 h exposure to UV irradiation and 90% after 1000 h in ambient air.

2. Results and discussion

Fig. 1a shows the scanning electron microscopy (SEM) image of the solution-processed C_{60} film which has voids and does not completely cover the indium-doped tin oxide (ITO) surface due to the inherently poor solubility of fullerene. In contrast, a layer of ultrathin-TiO_x (u-TiO_x) assists the C_{60}/u-TiO_x bilayer in fully covering the ITO surface (Fig. 1b). UV-vis transmittance spectra (Fig. S1a, ESI†) show that both the C_{60} layer and the C_{60}/u-TiO_x bilayer have high transparency in the visible wavelength range that would enable a high photon-flux to be harvested by active layers in solar cells. In addition, the energy levels of the C_{60}/u-TiO_x bilayer are determined by ultraviolet photoelectron spectroscopy (UPS) measurements. The valence band edges and band gaps for the C_{60}/u-TiO_x bilayer are conjointly used to derive the energy band diagrams in Fig. S1b (ESI†). The conduction band edge of the bilayer is positioned at −4.2 eV,

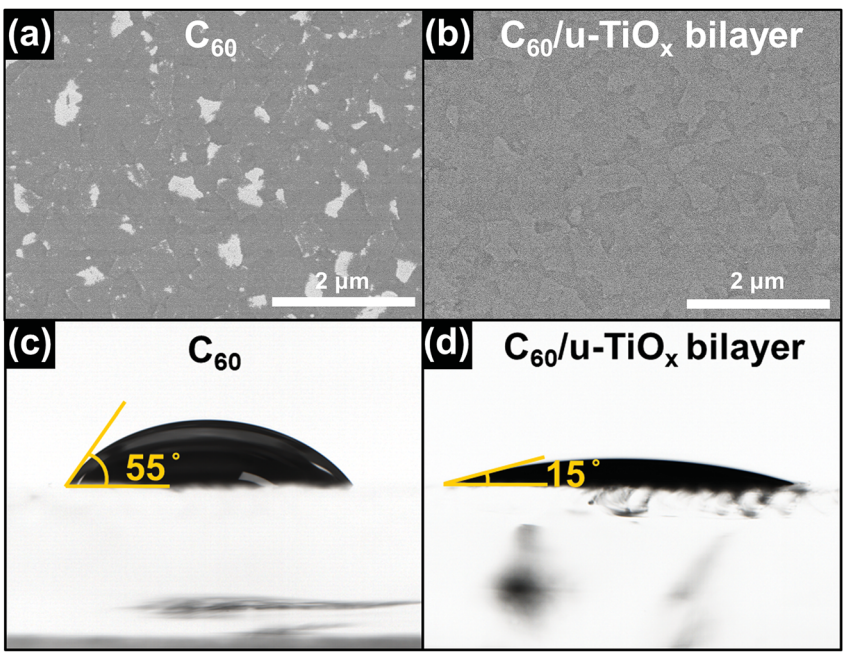

Fig. 1 Scanning electron microscopy (SEM) images of the (a) C_{60} layer and (b) C_{60}/u-TiO_x bilayer on ITO. And the perovskite precursor contact angle of (c) C_{60} and (d) C_{60}/u-TiO_x substrates.

much more optimally than that (−4.5 eV) of the C_{60} single layer as reported previously.[20] The more suitable band alignment efficiently reduces the energy level gap between the ITO and perovskite layer and also facilitates more efficient electron collection.[24] To closely observe the surface energy of ETLs, we measured the perovskite precursor contact angle on different substrates as shown in Fig. 1c and d. As expected,[25,26] the C_{60}/u-TiO_x bilayer promptly decreased the contact angle of the $FA_{0.85}MA_{0.15}PbI_{0.85}Br_{0.15}$ precursor on ETLs to 15°, much smaller than that (55°) of the C_{60} single layer. The incorporation of an ultrathin TiO_x film increases the wettability of the C_{60} film, which could be due to the increased surface energy of the bilayer in the presence of the hydrophilic TiO_x surface.[18,27–29]

The 70% improved wettability of ETLs for the perovskite precursor displayed an extraordinarily high surface energy of the bilayer, which avoids the rapid shrinking of the as-casted perovskite films during the annealing process. The pinholes in the solution-processed perovskite film on the C_{60} ETL are clearly visible at low magnification (Fig. 2a and b), and are serious defects in the active layer. Being consistent with a previous report,[30] when the size of the cell was increased to 9 cm^2, the loss of homogeneity and poorer coverage of the perovskite film on the C_{60} ETL are more severe in contrast to that on the C_{60}/u-TiO_x bilayer as shown in the insets of Fig. 2a and b. To quantify the electron trap-state density in the perovskite films on different substrates, space-charge-limited-currents (SCLC) of electron-only devices were measured as a function of voltage between 0.1 and 1.2 V in the dark (Fig. 2c). The *I–V* curves can be divided into three regions: the linear ohmic response region at the low bias voltage (orange line), the trap-filling region (green line) and the trap-free SCLC region. The trap-state density (N_t) of the film is determined from the trap-filled limit voltage (V_{TFL}) using the following equation.[13,31–35]

$$N_t = \frac{2\varepsilon_r\varepsilon_0 V_{TFL}}{qL^2} \quad (1)$$

where ε_r is the relative dielectric constant of the perovskite, ε_0 is the vacuum permittivity, q is the elemental charge, and L is the thickness of the film. With the V_{TFL} reducing from 0.88 V to 0.63 V, the trap densities of perovskite films decrease from 3.1 × 10^{16} cm^{-3} to 2.2 × 10^{16} cm^{-3} when C_{60}/u-TiO_x bilayers are introduced to replace C_{60} as ETLs. These observations are consisted with those of a previously reported perovskite deposited on different substrates.[13,34] The decreased trap densities confirm that the perovskite nucleation and growth process are partially dependent on the surface energy of the substrates.[36] According to the X-ray diffraction (XRD) patterns (Fig. 2d), the low trap-density perovskite film on the C_{60}/u-TiO_x bilayer indeed has higher crystallinity, which could suppress the charge recombination and facilitate the charge transport.[37]

The cross-sectional SEM images of the devices based on these ETLs reveal the effect of the u-TiO_x layer on both C_{60} and perovskite film formation. It is clear from Fig. 3a that discontinuation of the C_{60} film and migrated fullerene particles (marking with circles) occurred at several positions in the C_{60}-based PSC. In addition, C_{60} particles were even found to migrate from the bottom to the surface of the perovskite film in some parts of samples without the u-TiO_x layer in Fig. S2a and b.† This migration is mainly attributed to the dissolution of the

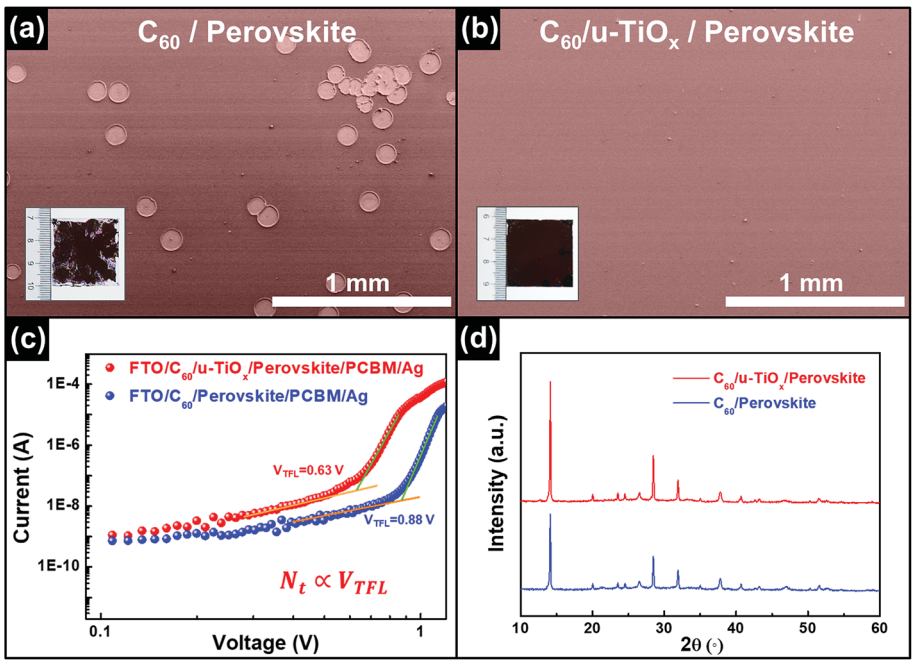

Fig. 2 SEM images with different scales of the perovskite films deposited on the (a) C_{60} layer and (b) C_{60}/u-TiO_x bilayer. Insets shown in (a, b) are the images of large-size (9 cm^2) perovskite films deposited on different substrates. (c) Dark current–voltage curves of the electron-only device revealing V_{TFL} inflection point behavior. (d) XRD patterns of perovskite films on the C_{60} layer and C_{60}/u-TiO_x bilayer.

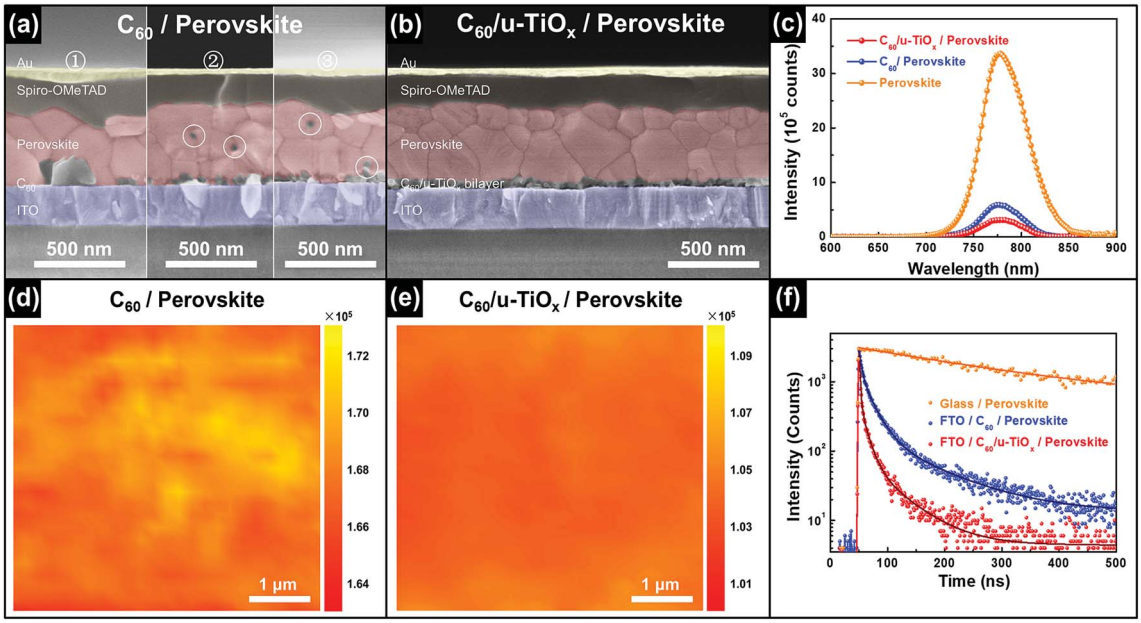

Fig. 3 Cross-sectional SEM images of (a) three positions in the C_{60}-based PSC and (b) the C_{60}/u-TiO_x bilayer-based PSC. (c) Steady-state photoluminescence (PL) spectra of perovskite films deposited on glass, C_{60} and the C_{60}/u-TiO_x bilayer. Confocal PL mapping intensity of perovskite films deposited on (d) C_{60} and (e) the C_{60}/u-TiO_x bilayer. (f) Time-resolved photoluminescence (TRPL) spectra of perovskite films deposited on glass, C_{60} and the C_{60}/u-TiO_x bilayer.

underlying C_{60} ETL by the anti-solvent during the spin-coating process of the perovskite. Thus the introduction of the u-TiO_x layer effectively prevents damage by chlorobenzene as a blocking layer as shown in Fig. 3b. Pinholes among the grain boundaries and gaps at the interface are also evident in the C_{60}-based structure, which may be induced by the low surface energy of the C_{60} film and are likely to act as significant traps in the active layer and the device. In contrast, the perovskite film crystallized on the designed C_{60}/u-TiO_x bilayer is homogeneous, smooth and pinhole-free. The efficiently reduced surface, bulk and interface defects are expected to suppress the charge recombination as discussed below.

Furthermore, steady-state photoluminescence (PL) measurement was conducted and is displayed in Fig. 3c. It has been demonstrated that PL quenching ratios are calculated to be 84% and 91% for C_{60} and C_{60}/u-TiO_x bilayer films respectively. This increase provides strong evidence that the bilayer efficiently accelerates the interfacial charge separation and charge collection.[38] We applied confocal PL mapping on the perovskite films deposited on the C_{60} and C_{60}/u-TiO_x bilayer substrates to visually characterize the carrier extraction and the emission distribution.[39,40] In the PL intensity maps (Fig. 3d and e), the C_{60}-based sample shows a higher absolute intensity and substantial heterogeneity in the emission, consistent with the PL data in Fig. 3c. In contrast, a more uniform emission distribution is observed by using the C_{60}/u-TiO_x bilayer as the ETL, and the lower PL intensity suggests that more carriers are able to reach the quenching layer. Fig. 3f shows the time-resolved PL decay (TRPL) results for perovskite samples on different substrates (glass, C_{60}, and C_{60}/u-TiO_x bilayer) to investigate the photo-induced carrier kinetics at the perovskite/ETL interface and the detailed lifetime is calculated in Table S1 (ESI†). For the C_{60} sample, the fast lifetime τ_1 is calculated to be 15.1 ns and the average lifetime τ_{ave} is calculated to be 68.3 ns. When the bilayer is introduced as the ETL, the τ_1 and τ_{ave} rapidly dropped to 9.4 ns and 63.3 ns, respectively. The C_{60}/u-TiO_x bilayer sample provides faster emission quenching than the C_{60} sample, resulting from higher electron injection efficiency and leading to superior photovoltaic performance.

As per quasi-equilibrium measurement, the open-circuit photovoltage decays (OCVD) could extract the slow phenomena at a characteristic time longer than ~10 ms from the hierarchical recombination process spanning many orders of magnitude in time. We fabricated devices with the configuration shown in Fig. 4a and measured the OCVD for different ETL based devices. The exponential decay distribution for OCVD in Fig. 4b reveals that the charge transfer in the PSCs is mediated by trapping and de-trapping processes. The V_{oc} decay time constant in the bilayer-based device (0.88 ms), fitting from OCVD curves, was measured to be ~6 times longer than that (0.14 ms) of the C_{60}-based device. That is to say, the charge transfer delay by trapping and de-trapping in the C_{60}-based device illustrates that it suffers from more variation of the Fermi level at the trap position and more energy loss of electronic states.[41,42] The trap densities of the devices are evidenced by the results of electron lifetime (Fig. 4c) calculated from OCVD measurement, as follows:

$$\tau_n = -\frac{k_B T}{e}\left(\frac{dV_{oc}}{dt}\right)^{-1} \quad (2)$$

where e, T and k_B are the elementary charge, the temperature and the Boltzmann constant, respectively.[42] Corresponding to

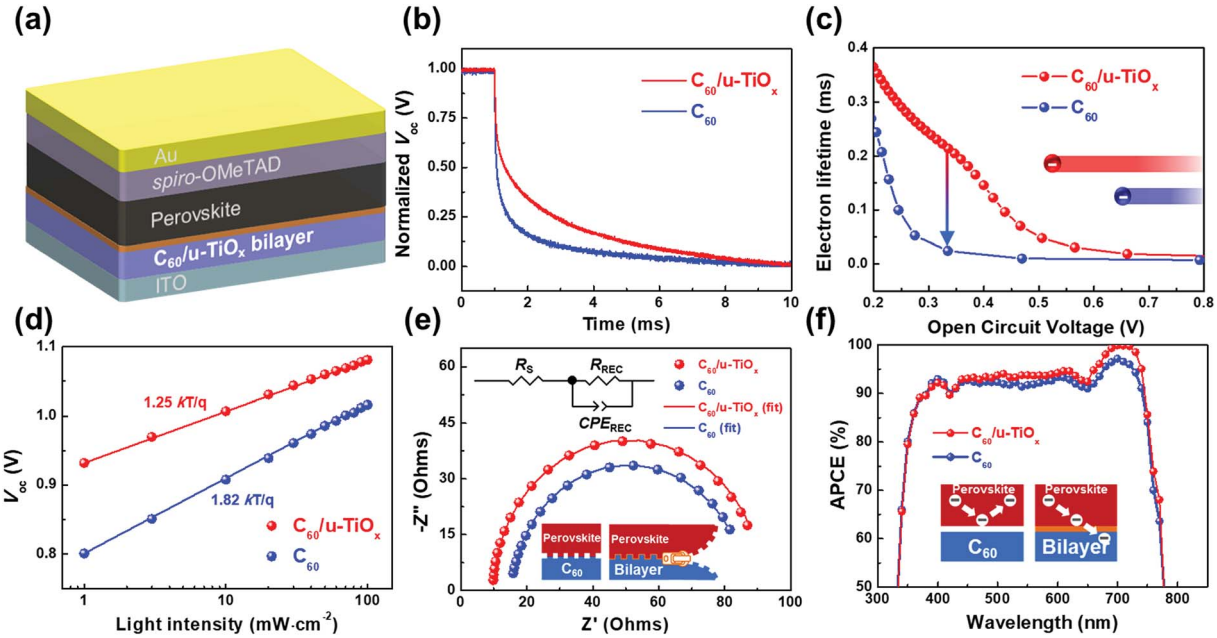

Fig. 4 (a) The schematic structure of a planar PSC based on the C_{60}/u-TiO_x bilayer ETL. (b) Transient photovoltage decay curves of C_{60} and C_{60}/u-TiO_x bilayer-based devices. (c) The calculated electron lifetimes and (d) V_{oc} as a function of light intensity for planar PSCs with C_{60} and C_{60}/u-TiO_x bilayer ETLs. (e) Representative Nyquist plots and (f) adsorbed photon-to-electron conversion efficiency of C_{60} and C_{60}/u-TiO_x bilayer-based PSCs.

the slower photovoltage decay, C_{60}/u-TiO_x bilayer-based PSCs prolong the electron lifetime (τ_n) over the same voltage region compared with the C_{60}-based device. The improvement of τ_n suggests the removal of the traps hidden in the bulk of perovskite after the introduction of the u-TiO_x layer on the top of the C_{60} film.[19,43] Fig. 4d shows the ideality factors of PSCs based on different substrates which are calculated from the measurements of V_{oc} as a function of light intensity. The ideality factors of C_{60}/u-TiO_x bilayer-based PSCs (n = 1.25) are notably increased in contrast to those of the C_{60}-based device (n = 1.82), suggesting that the introduction of the bilayer considerably reduces the surface recombination and non-uniform recombination centers in the active layer following the Shockley–Read–Hall theory.[44,45]

Electrochemical impedance spectroscopy (EIS) is performed to examine the interfacial charge transport dynamics. Fig. 4e shows the Nyquist plots of PSCs incorporating different ETLs at an applied voltage of 0.8 V under 1 sun illumination conditions. When the C_{60}/u-TiO_x bilayer is introduced, the results of curve fitting reveal that the series resistance (R_S) is effectively reduced from 15.6 Ω to 9.8 Ω and the recombination resistance (R_{REC}) is increased from 70.6 Ω to 81.8 Ω compared to that of the C_{60}-based devices. The improved interface contact and reduced carrier recombination originate from the improved electronic contact of the perovskite/ETL interface, where the u-TiO_x performs as a "band-aid" to suture the "wounds" between C_{60} and perovskite layers.[37,46] This result is well matched with absorbed photon-to-current conversion efficiency (APCE) measurements. The APCE is calculated from the light harvesting efficiency (LHE) and external quantum efficiency (EQE) in Fig. S3 (ESI†) as follows:

$$\mathrm{APCE} = \varphi_{inj} \times \varphi_{coll} \quad (3)$$

where φ_{inj} and φ_{coll} are the electron injection and electron collection efficiencies, respectively.[47,48] The overall APCE of the C_{60}/u-TiO_x bilayer-based device in the wavelength range from 500 nm to 750 nm is estimated to be higher than that of the C_{60}-based device in Fig. 4f. The higher APCE is attributed to the faster electron injection, more efficient electron collection and less contactless-interface-induced charge recombination.

The optimal concentration of $TiCl_4$ solution was found by comparing the photovoltaic performance (Table S2, ESI†) of C_{60}/u-TiO_x bilayer-based PSCs with a $TiCl_4$ treatment process varying the solution concentration from 0 to 9 mM. The results reveal that the optimal concentration of $TiCl_4$ solution is 5 mM, and the corresponding device (1 cm^2) in reverse scan shows an open-circuit voltage (V_{oc}) of 1.10 V, a fill factor (FF) of 77.79%, a short-circuit current density (J_{sc}) of 22.64 mA cm^{-2}, and a PCE of 19.38%. The J_{sc} is in excellent agreement with the external quantum efficiencies (EQEs) shown in Fig. S4a (ESI†). Three types of PSCs are fabricated with TiO_2, C_{60} and theC_{60}/u-TiO_x bilayer as ETLs, respectively. The photocurrent–voltage (J–V) curves in both reverse and forward scanning directions for the optimized devices are measured under simulated AM 1.5G sun light at 100 mW cm^{-2} and shown in Fig. 5a and summarized in Table 1. It is noted that the C_{60}/u-TiO_x bilayer-based device has a higher V_{oc}, FF and ultra-low hysteresis index (HI), which may indicate better interfacial contact and lower defect densities.[49,50]

Notably, the histograms of efficiencies exhibit a tremendous difference between C_{60} and C_{60}/u-TiO_x bilayer-based devices in Fig. 5b. The extremely wide distribution of the PCE of C_{60}-based devices is mainly attributed to the pinhole-induced short-circuit

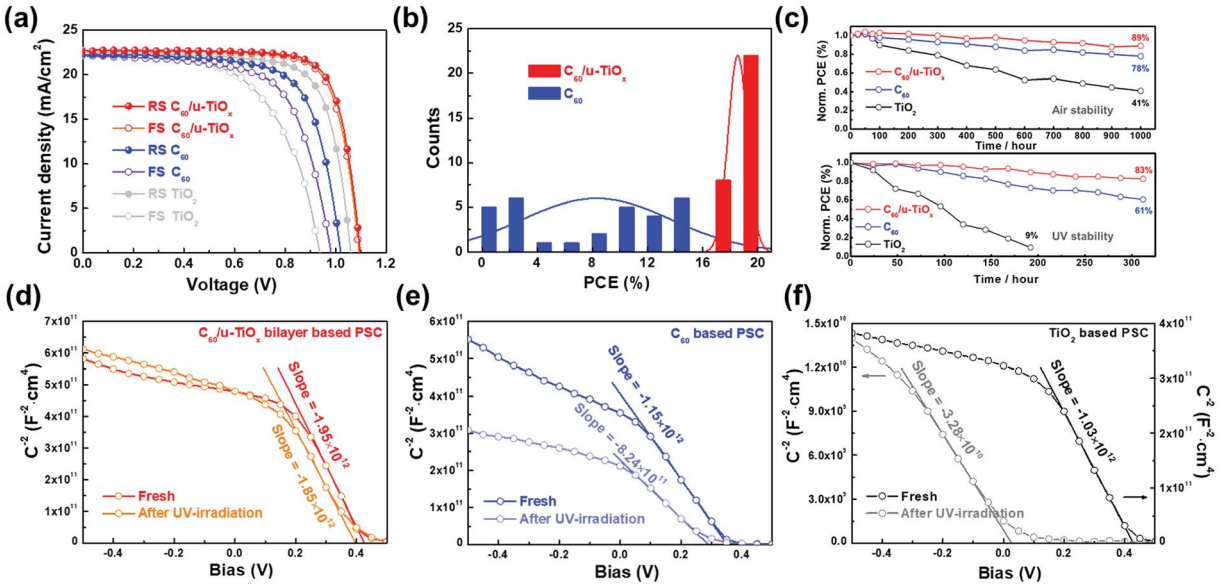

Fig. 5 (a) *J–V* curves of the best performing large-area (1 cm^2) devices with TiO_2, C_{60} and the C_{60}/u-TiO_x bilayer as ETLs, respectively. (b) Histograms of PCEs for 60 devices with different ETLs. (c) The evolution of the normalized PCEs of unsealed PSCs consisting of different ETLs under an ambient environment (≈45% humidity and 30 °C), with or without constant 10 mW cm^{-2} UV irradiation (λ = 340 nm). The Mott–Schottky plot of (d) C_{60}/u-TiO_x bilayer, (e) C_{60} and (f) TiO_2-based PSCs was obtained before and after UV irradiation at a 1 kHz probe frequency.

Table 1 Photovoltaic parameters of large-area (1 cm^2) devices fabricated with TiO_2, C_{60} and C_{60}/u-TiO_x bilayer ETLs measured under AM 1.5 illumination

		J_{sc} (mA cm^{-2})	V_{oc} (V)	FF (%)	PCE (%)	HI (%)
TiO_2	RS	22.42	1.06	74.07	17.62	15.79
	FS	22.43	0.94	59.10	12.43	
C_{60}	RS	22.25	1.02	70.15	15.93	6.12
	FS	22.11	0.98	66.19	14.38	
C_{60}/u-TiO_x	RS	22.64	1.10	77.79	19.38	0.85
	FS	22.75	1.09	76.47	19.01	

current of the devices and anti-solvent-induced random migration of C_{60} grains, while the ultrathin TiO_x effectively blocks the damage to the C_{60} ETL from the anti-solvent during the spin-coating process of the perovskite and further improves the repeatability of the devices. The steady-state photocurrent and PCE are measured at the maximum power point (MPPT) of the most efficient devices with different ETLs as shown in Fig. S4b (ESI†). The steady photocurrent and stabilized PCE of C_{60}/u-TiO_x bilayer-based solar cells measured at the MPPT are consistent with those measured from *J–V* scanning, eliminating the photocurrent hysteresis in the devices. The absence of hysteresis and quick response of C_{60}/u-TiO_x bilayer-based devices may be ascribed to the higher charge transport driven by the decrease of trap densities.

Stability is one of the most crucial requirements for PSCs. The long-term stability of unencapsulated PSCs has been evaluated under an ambient environment with a humidity of about 45% at room temperature under white light illumination (10 mW cm^{-2}). The performance of the devices was recorded periodically, and the normalized PCEs against time are shown in Fig. 5c. The initial PCE value of the C_{60}-based device remained unchanged for 100 h and then gradually reduced to approximate 78% in 1000 h. In contrast, the C_{60}/u-TiO_x bilayer-based device retained the initial PCE for nearly 300 h and maintained 89% of the initial PCE at 1000 h. However, the PCE of the TiO_2-based device decreased to 41% in 1000 h under the same exposure and testing conditions. To understand the degradation mechanism of different devices, a UV-light soaking (10 mW cm^{-2}, λ = 340 nm) experiment was conducted under the same ambient environment (humidity = ~45%) by monitoring the PCE characteristics of different PSCs as shown in Fig. 5c. Interestingly, the rankings of the devices in this UV-stability assessment did not change compared to the air-stability test, while the main difference was that the degradation under UV exposure is accelerated by the high energy of UV light. C_{60}/u-TiO_x bilayer and C_{60}-based PSCs retain 83% and 61% of their initial performance after UV irradiation for 312 hours, respectively, whereas the TiO_2-based cell completely degrades within 200 hours. The UV-stability of C_{60}/u-TiO_x bilayer-based PSCs is superior compared with previous reports.[18,51,52] Moreover, Fig. S5a–c† present the XRD patterns of different ETL-based perovskite films before and after exposure to an ambient environment and UV-irradiation for 312 h. The perovskite film on the bilayer showed a slight decomposition in the XRD patterns after the aging experiments, while the aged perovskite films on the TiO_2 ETL exhibited a noticeable PbI_2 main peak ($2\theta = 12.6°$), suggesting that changing the configuration of the ETL could largely vary the stability of the upper perovskite under air exposure and UV-light soaking. To further comprehend the role of UV light in the degradation, the Mott–Schottky (MS) plots for

different ETL-based PSCs were generated from the capacitance–voltage measurements, where the interfacial charge densities are inversely proportional to the slope of the MS plots.[53,54] Fig. 5d–f display the MS plots of different ETL-based devices before and after 5 h UV irradiation in air, where negligible PCE degradation of the devices (Fig. 5c) and no impurity in the perovskite films (Fig. S5d–f†) can be observed. Before the UV-irradiation, the slopes of the MS plots for different ETL-based devices were in the same order of magnitude. However, after the UV-irradiation for 5 h, the slope of the bilayer-based device is one and two orders of magnitude higher than that of C_{60} and TiO_2-based devices, respectively, indicating less interfacial charge accumulation and thus excellent charge extraction at the electrode interface for the bilayer devices. That is to say, the electrons passing through the ultrathin TiO_x have been instantly extracted and transported by the underlying C_{60} film in the bilayer structure. And it has been proved in previous reports that the absence of an ETL could induce a high interfacial charge density,[55] which explains the more obvious interfacial charge accumulation in the device based on the leaky C_{60} film than that on the bilayer. For the TiO_2-based device, upon UV radiation, numerous electrons that have not been extracted will be trapped into oxygen vacancies in the TiO_2 bulk and then may recombine with the photo-generated holes.[52,56] Thus the lower slope of the MS plot is likely to be attributed to the high trap density and low electron mobility of TiO_2 ETLs.[12,57] Additionally, the high charge accumulation at the TiO_2/perovskite interface helps to explain the severe hysteresis, which is considered to originate from capacitive current,[58] trapped charge[59] and unbalanced charge injection.[60] Given the above, both the air- and UV-related degradation characteristics of different PSCs are well consistent with a previous report,[21] indicating that the interfacial charge extraction between the ETL and perovskite film plays a key role in moisture-driven decomposition of perovskite films. And the interfacial charge accumulation may further strengthen the hydrogen interaction between the organic cation and H_2O under light illumination.[61] Fast extraction and transport of electrons through the C_{60}/u-TiO_x bilayer would hardly accumulate negative charges at the interface between the ETL and perovskite and effectively suppress the irreversible decomposition of perovskite materials.

To demonstrate the reproducibility of the C_{60}/u-TiO_x bilayer for PSCs, large-area (1 cm^2) PSCs were fabricated and their J–V performance was measured with a black metal mask under simulated AM 1.5 sunlight conditions. As shown in Fig. 6a, a high PCE of over 18.83% is obtained with a J_{sc} of 22.4 mA cm^{-2}, a V_{oc} of 1.09 V, and a FF of 77.0%. We also measured J–V curves with a small metal mask (each 0.3 cm by 0.3 cm) at five different positions located at the center and the four corners of the active area of the large-area device. All the PV metrics extracted from these five curves are almost identical, attesting to the superior uniformity of the perovskite film deposited on the C_{60}/u-TiO_x bilayer over the square-centimeter scale. The PSCs based on flexible polyethylene terephthalate/ultrathin (8 nm) gold (PETUG) substrates were also fabricated to evidence the viability of the C_{60}/u-TiO_x bilayer for flexible optoelectronic applications. Fig. 6b shows the digital camera image of the fabricated flexible perovskite solar cell with the structure (Fig. 6c) of PETUG/C_{60}/u-TiO_x/perovskite/2,2′,7,7′-tetrakis(*N*,*N*-

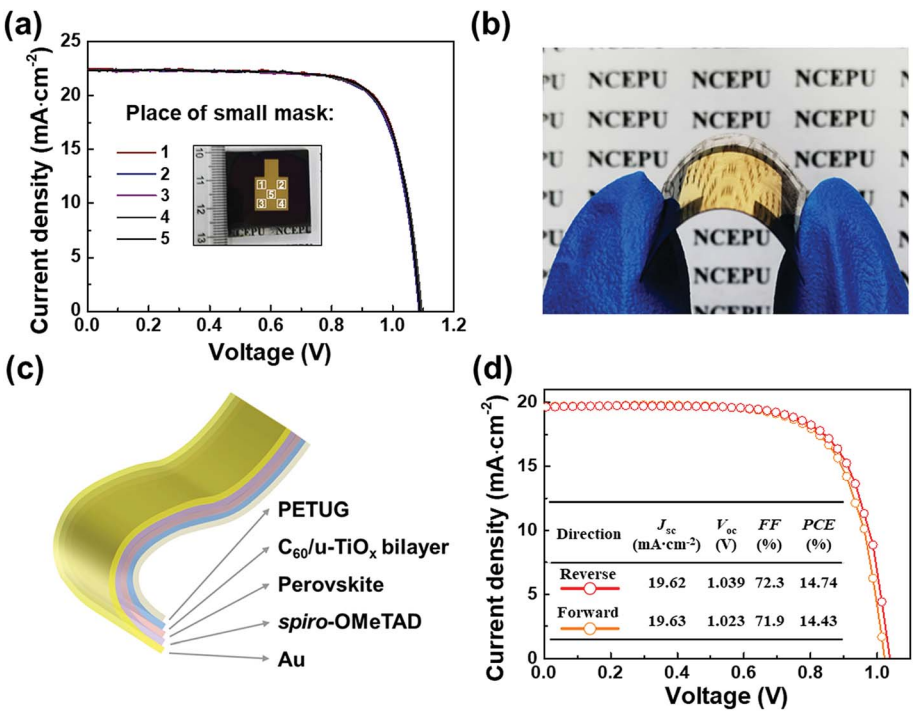

Fig. 6 (a) J–V curves measured from five different spots with an aperture area of 0.09 cm^2 selected from the large-area device (active area of 1.2 × 1.2 cm^2) as shown in the inset picture. (b) Device structure, (c) the photographs and (d) J–V curves of the large-area (1 cm^2) flexible PSCs.

di-*p*-methoxyphenylamine)-9,9′-spirobifluorene (spiro-OMeTAD)/Au. The key *J–V* curve of the best cell with an active area of 1 cm^2 exhibits a J_{sc} of 19.60 mA cm^{-2}, a V_{oc} of 1.04 V, and a FF of 72.3%, giving a PCE of 14.74% (Fig. 6d). The lower PCE in contrast to that of the rigid device is likely due to the higher series resistance and lower transmittance of the PETUG substrate (Fig. S5, ESI†).[13,62] The flexible device even retained nearly 92% of its initial PCE after 200 bending cycles, indicating good mechanical stability.

3. Conclusion

A C_{60}/u-TiO_x bilayer is introduced to fully cover the electrode, improve the surface energy of the ETL and prevent the attack on C_{60} by chlorobenzene anti-solvent. The charge transport and electron extraction are greatly enhanced due to the intimate interfacial contact between the ETL and perovskite layer. The bilayer also benefits the growth of a high-quality and reduced-defect perovskite film, resulting in suppressed charge carrier recombination in the whole device. Based on these improvements, the large-area (1 cm^2) PSC with rigid and flexible substrates shows a PCE of 19.38% and 14.74%, respectively. Most importantly, because fast extraction and transport of electrons through the C_{60}/u-TiO_x bilayer would hardly accumulate negative charges at the interface between the ETL and perovskite and effectively suppress the irreversible moisture-driven decomposition of perovskite materials, the long-term stability of the C_{60}/u-TiO_x bilayer-based device has been remarkably improved under the exposure of both ambient air and UV-irradiation. The development of C_{60}/u-TiO_x bilayers moves us a step closer to the commercialization of PSCs by significantly enhancing the durability of photovoltaic devices.

Conflicts of interest

There are no conflicts to declare.

Acknowledgements

This work was supported by the National Key Research and Development Program of China (No. 2016YFA0202400), the 111 Project (No. B16016), the National Natural Science Foundation of China (No. U1705256 and 51702096), and The Double top construction Program of North China Electric Power University (No. XM1805314).

References

1 W. S. Yang, B.-W. Park, E. H. Jung, N. J. Jeon, Y. C. Kim, D. U. Lee, S. S. Shin, J. Seo, E. K. Kim and J. H. Noh, *Science*, 2017, **356**, 1376–1379.
2 M. Cai, N. Ishida, X. Li, X. Yang, T. Noda, Y. Wu, F. Xie, H. Naito, D. Fujita and L. Han, *Joule*, 2018, **2**, 296–306.
3 N. J. Jeon, H. Na, E. H. Jung, T.-Y. Yang, Y. G. Lee, G. Kim, H.-W. Shin, S. I. Seok, J. Lee and J. Seo, *Nat. Energy*, 2018, **3**, 682.
4 D. Liu and T. L. Kelly, *Nat. Photonics*, 2014, **8**, 133–138.
5 Q. Jiang, Z. Chu, P. Wang, X. Yang, H. Liu, Y. Wang, Z. Yin, J. Wu, X. Zhang and J. You, *Adv. Mater.*, 2017, **29**, 1703852.
6 X. Liu, K. W. Tsai, Z. Zhu, Y. Sun, C. C. Chueh and A. K. Y. Jen, *Adv. Mater. Interfaces*, 2016, **3**, 1600122.
7 S. S. Shin, W. S. Yang, J. H. Noh, J. H. Suk, N. J. Jeon, J. H. Park, J. S. Kim, W. M. Seong and S. I. Seok, *Nat. Commun.*, 2015, **6**, 7410.
8 B. Roose, J.-P. C. Baena, K. C. Gödel, M. Graetzel, A. Hagfeldt, U. Steiner and A. Abate, *Nano Energy*, 2016, **30**, 517–522.
9 K. Wang, Y. Shi, Q. Dong, Y. Li, S. Wang, X. Yu, M. Wu and T. Ma, *J. Phys. Chem. Lett.*, 2015, **6**, 755–759.
10 H. Kim, K.-G. Lim and T.-W. Lee, *Energy Environ. Sci.*, 2016, **9**, 12–30.
11 S. S. Shin, E. J. Yeom, W. S. Yang, S. Hur, M. G. Kim, J. Im, J. Seo, J. H. Noh and S. I. Seok, *Science*, 2017, **356**, 167–171.
12 G. Yang, H. Tao, P. Qin, W. Ke and G. Fang, *J. Mater. Chem. A*, 2016, **4**, 3970–3990.
13 D. Yang, R. Yang, X. Ren, X. Zhu, Z. Yang, C. Li and S. Liu, *Adv. Mater.*, 2016, **28**, 5206–5213.
14 W. Chen, Y. Wu, Y. Yue, J. Liu, W. Zhang, X. Yang, H. Chen, E. Bi, I. Ashraful and M. Grätzel, *Science*, 2015, **350**, 944–948.
15 Y. H. Hu and E. Ruckenstein, *J. Am. Chem. Soc.*, 2005, **127**, 11277–11282.
16 M. S. Dresselhaus, G. Dresselhaus and P. C. Eklund, *Science of fullerenes and carbon nanotubes: their properties and applications*, Elsevier, 1996.
17 K. Wojciechowski, T. Leijtens, S. Siprova, C. Schlueter, M. T. Hörantner, J. T.-W. Wang, C.-Z. Li, A. K.-Y. Jen, T.-L. Lee and H. J. Snaith, *J. Phys. Chem. Lett.*, 2015, **6**, 2399–2405.
18 C. Liu, Y. Yang, Y. Ding, J. Xu, X. Liu, B. Zhang, J. Yao, T. Hayat, A. Alsaedi and S. Dai, *ChemSusChem*, 2018, **11**, 1232–1237.
19 W. Ke, D. Zhao, C. R. Grice, A. J. Cimaroli, J. Ge, H. Tao, H. Lei, G. Fang and Y. Yan, *J. Mater. Chem. A*, 2015, **3**, 17971–17976.
20 H. Yoon, S. M. Kang, J.-K. Lee and M. Choi, *Energy Environ. Sci.*, 2016, **9**, 2262–2266.
21 N. Ahn, K. Kwak, M. S. Jang, H. Yoon, B. Y. Lee, J.-K. Lee, P. V. Pikhitsa, J. Byun and M. Choi, *Nat. Commun.*, 2016, **7**, 13422.
22 A. Yella, L.-P. Heiniger, P. Gao, M. K. Nazeeruddin and M. Grätzel, *Nano Lett.*, 2014, **14**, 2591–2596.
23 B. J. Kim, D. H. Kim, Y.-Y. Lee, H.-W. Shin, G. S. Han, J. S. Hong, K. Mahmood, T. K. Ahn, Y.-C. Joo and K. S. Hong, *Energy Environ. Sci.*, 2015, **8**, 916–921.
24 M. M. Tavakoli, F. Giordano, S. M. Zakeeruddin and M. Grätzel, *Nano Lett.*, 2018, **18**, 2428–2434.
25 Z. Wang, D. P. Mcmeekin, N. Sakai, R. S. Van, K. Wojciechowski, J. B. Patel, M. B. Johnston and H. J. Snaith, *Adv. Mater.*, 2016, **29**, 1604186.
26 M. R. Ahmadian-Yazdi, A. Rahimzadeh, Z. Chouqi, Y. Miao and M. Eslamian, *AIP Adv.*, 2018, **8**, 025109.
27 J. Kim, H. Lee, H. P. Kim, T. Lin, A. Kanwat, A. R. B. Mohd Yusoff and J. Jang, *Nanoscale*, 2016, **8**, 9284–9292.

28 X. Xu, C. Ma, Y. Cheng, Y. M. Xie, X. Yi, B. Gautam, S. Chen, H. W. Li, C. S. Lee and F. So, *J. Power Sources*, 2017, **360**, 157–165.
29 Q. Wei, Y. Zhou, Y. Dong, Z. Wei, X. Ren, Y. Liu, X. Liu, J. Feng and S. Liu, *Sol. Energy*, 2016, **135**, 654–661.
30 K. M. Lee, C. C. Chen, L. C. Chen, S. H. Chang, K. S. Chen, S. C. Yeh, C. T. Chen and C. G. Wu, *Sol. Energy Mater. Sol. Cells*, 2017, **164**, 13–18.
31 F. Cai, Y. Yan, J. Yao, P. Wang, H. Wang, R. S. Gurney, D. Liu and T. Wang, *Adv. Funct. Mater.*, 2018, 1801985.
32 R. H. Bube, *J. Appl. Phys.*, 1962, **33**, 1733–1737.
33 T. Niu, J. Lu, R. Munir, J. Li, D. Barrit, X. Zhang, H. Hu, Z. Yang, A. Amassian and K. Zhao, *Adv. Mater.*, 2018, **30**, 1706576.
34 F. Cai, L. Yang, Y. Yan, J. Zhang, F. Qin, D. Liu, Y.-B. Cheng, Y. Zhou and T. Wang, *J. Mater. Chem. A*, 2017, **5**, 9402–9411.
35 D.-Y. Son, S.-G. Kim, J.-Y. Seo, S.-H. Lee, H. Shin, D. Lee and N.-G. Park, *J. Am. Chem. Soc.*, 2018, **140**, 1358–1364.
36 Z. Arain, C. Liu, Y. Yang, M. Mateen, Y. Ren, Y. Ding, X. Liu, Z. Ali, M. Kumar and S. Dai, *Sci. China Mater.*, 2019, **62**, 161–172.
37 T. Cao, H. Peng, K. Zhang, Z. Sun, Z. Kai, L. Yuan, C. Kang, C. Ning and Y. Li, *J. Mater. Chem. A*, 2018, **6**, 3435–3443.
38 H. H. Fang, J. Yang, S. Tao, S. Adjokatse, M. E. Kamminga, J. Ye, G. R. Blake, J. Even and M. A. Loi, *Adv. Funct. Mater.*, 2018, **28**, 1800305.
39 Y. Yang, H. Peng, C. Liu, Z. Arain, Y. Ding, S. Ma, X. Liu, T. Hayat, A. Alsaedi and S. Dai, *J. Mater. Chem. A*, 2019, **7**, 6450–6458.
40 M. Long, T. Zhang, M. Liu, Z. Chen, C. Wang, W. Xie, F. Xie, J. Chen, G. Li and J. Xu, *Adv. Mater.*, 2018, **30**, e1801562.
41 J. Bisquert, A. Zaban, M. Greenshtein and I. Mora-Seró, *J. Am. Chem. Soc.*, 2004, **126**, 13550–13559.
42 A. Zaban, M. Greenshtein and J. Bisquert, *ChemPhysChem*, 2003, **4**, 859–864.
43 X. Jia, Y. Jian, X. Li, Z. Bing, J. Yao and S. Dai, *Sol. Energy Mater. Sol. Cells*, 2016, **157**, 1026–1037.
44 O. Almora, K. T. Cho, S. Aghazada, I. Zimmermann, G. J. Matt, C. J. Brabec, M. K. Nazeeruddin and G. Garcia-Belmonte, *Nano Energy*, 2018, **48**, 63–72.
45 T. Du, J. Kim, J. Ngiam, S. Xu, P. R. Barnes, J. R. Durrant and M. A. McLachlan, *Adv. Funct. Mater.*, 2018, **28**, 1801808.
46 L. L. Jiang, Z. K. Wang, M. Li, C. C. Zhang, Q. Q. Ye, K. H. Hu, D. Z. Lu, P. F. Fang and L. S. Liao, *Adv. Funct. Mater.*, 2018, **28**, 1705875.
47 Y. Rong, Z. Ku, A. Mei, T. Liu, M. Xu, S. Ko, X. Li and H. Han, *J. Phys. Chem. Lett.*, 2014, **5**, 2160–2164.
48 J.-W. Lee, S. H. Lee, H.-S. Ko, J. Kwon, J. H. Park, S. M. Kang, N. Ahn, M. Choi, J. K. Kim and N.-G. Park, *J. Mater. Chem. A*, 2015, **3**, 9179–9186.
49 J.-W. Lee, S.-G. Kim, S.-H. Bae, D.-K. Lee, O. Lin, Y. Yang and N.-G. Park, *Nano Lett.*, 2017, **17**, 4270–4276.
50 J. Chen, J. Xu, S. Zhang, S. Zhou, K. Zhou, B. Zhang, X. Xia, Y. Liu, S. Dai and J. Yao, *J. Phys. Chem. C*, 2017, **121**, 28443–28453.
51 T. E. Chen, C. E. Lin, S. I. Li, Y. Tsai, C. E. Wen, W. J. Lin, F. A. Hsiao, Y. I. Chiu, K. Tsukagoshi and M. Osada, *Adv. Energy Mater.*, 2018, **8**, 1701722.
52 W. Li, W. Zhang, S. Van Reenen, R. J. Sutton, J. Fan, A. A. Haghighirad, M. B. Johnston, L. Wang and H. J. Snaith, *Energy Environ. Sci.*, 2016, **9**, 490–498.
53 F. Cai, J. Cai, L. Yang, W. Li, R. S. Gurney, H. Yi, A. Iraqi, D. Liu and T. Wang, *Nano Energy*, 2018, **45**, 28–36.
54 K. Wojciechowski, S. D. Stranks, A. Abate, G. Sadoughi, A. Sadhanala, N. Kopidakis, G. Rumbles, C. Z. Li, R. H. Friend, A. K. Y. Jen and H. J. Snaith, *ACS Nano*, 2014, **8**, 12701–12709.
55 L. Yao, M. Bag, L. A. Renna, Z. A. Page and T. P. Russell, *Adv. Energy Mater.*, 2016, **6**, 1501606.
56 T. Leijtens, G. E. Eperon, S. Pathak, A. Abate, M. M. Lee and H. J. Snaith, *Nat. Commun.*, 2013, **4**, 2885.
57 S. Gubbala, V. Chakrapani, V. Kumar and M. K. Sunkara, *Adv. Funct. Mater.*, 2008, **18**, 2411–2418.
58 H. S. Kim, I. H. Jang, N. Ahn, M. Choi, A. Guerrero, J. Bisquert and N. G. Park, *J. Phys. Chem. Lett.*, 2015, **6**, 4633–4639.
59 B. Chen, M. Yang, S. Priya and K. Zhu, *J. Phys. Chem. Lett.*, 2016, **7**, 905–917.
60 W. Tress, N. Marinova, T. Moehl, S. M. Zakeeruddin, M. K. Nazeeruddin and M. Grätzel, *Energy Environ. Sci.*, 2015, **8**, 995–1004.
61 J. A. Christians, P. A. M. Herrera and P. V. Kamat, *J. Am. Chem. Soc.*, 2015, **137**, 1530–1538.
62 Z. Wu, P. Li, Y. Zhang and Z. Zheng, *Small Methods*, 2018, **2**, 1800031.